

Spring Mixing: Turbulence and Internal Waves during Restratification on the New England Shelf

J. A. MACKINNON

Scripps Institution of Oceanography, University of California, San Diego, La Jolla, California

M. C. GREGG

Applied Physics Laboratory, and School of Oceanography, University of Washington, Seattle, Washington

(Manuscript received 16 June 2004, in final form 12 May 2005)

ABSTRACT

Integrated observations are presented of water property evolution and turbulent microstructure during the spring restratification period of April and May 1997 on the New England continental shelf. Turbulence is shown to be related to surface mixed layer entrainment and shear from low-mode near-inertial internal waves. The largest turbulent diapycnal diffusivity and associated buoyancy fluxes were found at the bottom of an actively entraining and highly variable wind-driven surface mixed layer. Away from surface and bottom boundary layers, turbulence was systematically correlated with internal wave shear, though the nature of that relationship underwent a regime shift as the stratification strengthened. During the first week, while stratification was weak, the largest turbulent dissipation away from boundaries was coincident with shear from mode-1 near-inertial waves generated by passing storms. Wave-induced Richardson numbers well below 0.25 and density overturning scales of several meters were observed. Turbulent dissipation rates in the region of peak shear were consistent in magnitude with several dimensional scalings. The associated average diapycnal diffusivity exceeded $10^{-3} \text{ m}^2 \text{ s}^{-1}$. As stratification tripled, Richardson numbers from low-mode internal waves were no longer critical, though turbulence was still consistently elevated in patches of wave shear. Kinematically, dissipation during this period was consistent with the turbulence parameterization proposed by MacKinnon and Gregg, based on a reinterpretation of wave-wave interaction theory. The observed growth of temperature gradients was, in turn, consistent with a simple one-dimensional model that vertically distributed surface heat fluxes commensurate with calculated turbulent diffusivities.

1. Introduction

Marking a fundamental boundary between the human and marine environments, continental shelves are vital and vibrant places where high biological productivity is coincident with, and at times threatened by, commercial fisheries, pollution, and other human activities. Turbulent mixing is a crucial mechanism controlling the distribution of physical water properties, nutrient fluxes, and concentrations of particulate matter on shelves (Sandstrom and Elliot 1984; Aikman 1984; Sharples et al. 2001). Turbulent mixing may be triggered by surface wind stress, frictional drag against

the bottom, or dynamical instability of internal waves in stratified water. Turbulence, in turn, drains energy from the internal wave field and controls local stratification by redistributing heat and salt within the water column.

Many previous studies of mixing on shelves focused on turbulence generated by frictional boundary processes (Dewey and Crawford 1988; Simpson et al. 1996; Shaw et al. 2001; Nash and Moum 2001). On the other hand, Simpson et al. (1996), Inall et al. (2000), and Rippeth and Inall (2002) discover strong turbulence in the thermocline that is inconsistent with generation by surface or bottom stresses. In fact, even mild stratification can limit the vertical range of boundary layers; turbulent fluxes through the pycnocline are then controlled by internal dynamics, which often are internal wave instabilities. In particular, most previous studies of internal waves and mixing in coastal regions have

Corresponding author address: Jennifer MacKinnon, SIO, UCSD, 9500 Gilman Drive, Mail Code 0213, La Jolla, CA 92093-0213.

E-mail: jen@coast.ucsd.edu

focused on the role of the internal tide, especially its nonlinear (soliton) incarnation (Sandstrom and Elliot 1984; Sandstrom and Oakey 1995; Holloway et al. 2001; Colosi et al. 2001; Moum et al. 2003).

Wind-generated near-inertial internal waves are also a common feature on shelves (Chen et al. 1996; Chen and Xie 1997; Chant 2001). Yet, comparatively little work has been done relating mixing to near-inertial waves on shelves, though near-inertial shear has been shown to play a vital role in the open-ocean thermocline turbulence (Hebert and Moum 1994; Alford and Gregg 2001). Van Haren et al. (1999) show that, as springtime stratification strengthens in the North Sea, the magnitude of near-inertial waves and associated turbulent fluxes also grow, and provide an important feedback to evolving stratification.

The Coastal Mixing and Optics (CMO) project integrated comprehensive measurements of wave shear, stratification, and turbulent dissipation on the New England shelf during the late summer 1996 and spring 1997. Full reports on the hydrographic, optical, and biological context are presented in a special issue of *Journal of Geophysical Research* (2001, Vol. 106, No. C5; Dickey and Williams 2001).

Two previous papers by the present authors (MacKinnon and Gregg 2003b, hereinafter MGb; MacKinnon and Gregg 2003a, hereinafter MGa) discussed the internal wave field and associated turbulent dissipation observed in late summer 1996. They found that baroclinic energy was dominated by a variable internal tide, episodic nonlinear solitons, and near-inertial internal waves. In this strongly stratified environment (average buoyancy frequency of 11 cph), the surface (bottom) mixed layer was limited to 5 (10) m. Half of the turbulent dissipation in the thermocline occurred during soliton passage and was linked to strong shear in these mode-1 waves. The remaining turbulent dissipation was positively correlated with both stratification and low-mode, low-frequency shear. They found that a common class of successful open-ocean turbulence parameterization failed to reproduce observed relationships between dissipation, shear, and stratification and proposed a new parameterization consistent with the coastal wave field (further details in section 4). Other summer CMO measurements from both microstructure (Oakey and Greenan 2004) and purposeful dye release studies (Ledwell et al. 2004) show similar low average dissipation and diffusivity rates that fall within the bounds of the parameterization proposed by MGa.

The spring 1997 component of the CMO experiment provided an opportunity to extend the dynamic insights

and kinematic parameterizations of previous work to an environment that was distinct in at least two fundamental ways. First, there was no sign of an internal tide in the spring. Instead baroclinic energy predominantly came from near-inertial internal waves linked to wind stress from passing storms (Shearman 2005). Second, the tripling of average stratification over the fortnight of observations (mostly due to local solar heating) provided an opportunity to study the evolution of internal-wave-related turbulence and associated parameterizations, through a variety of dynamic regimes.

A companion paper, MacKinnon and Gregg (2005, hereinafter MG05), tackles the generation and evolution of internal waves in response to local forcing. In this paper, we focus on turbulent dissipation and the impact of associated mixing on evolving water properties. We begin in section 2 with a description of the experimental details and measurement techniques. Detailed descriptions of evolving water properties and observed patterns of turbulence are given in section 3. Analysis is separated into three hydrodynamic zones: the surface mixed layer, the bottom mixed layer, and the continuously stratified (“midcolumn”) region in between. In section 4 we focus on midcolumn mixing; discuss the relationship between observed turbulence, stratification and internal wave shear; and evaluate several turbulence parameterizations. We discuss the context of these mixing patterns in section 5, by comparison with regional and global measurements, and evaluate the impacts and importance of turbulent mixing on the shelf. A simple one-dimensional model of mixing based on observed turbulence patterns is proposed and successfully reproduces most features of the evolving spring restratification. Conclusions are presented in section 6.

2. Experimental methods

a. Overview

The experimental details are described fully in MG05; only the main salient details are mentioned here. From 26 April to 12 May 1997, we obtained microstructure, acoustic Doppler current profiler (ADCP), and echosounder data near the 70-m isobath south of Nantucket Island, Massachusetts. We were forced to return to shore twice during this interval, resulting in gaps in the data. Although profiler quantities are measured as a function of pressure, here all quantities are plotted versus depth, which produces an average error of less than 1% for the depth range measured. Meteorological data and calculated quantities (wind stress, heat flux) are primarily from the improved

meteorological (IMET) sensor onboard the R/V *Knorr* and are provided courtesy of the Woods Hole Oceanographic Institution (WHOI).

b. Microstructure

Our primary instrument was the Modular Microstructure Profiler (MMP), a loosely tethered free-falling instrument ballasted to sink at a rate of 50 cm s^{-1} . A complete water column profile took approximately four minutes during peak operating efficiency, resulting in 2195 total profiles. The MMP is equipped with SeaBird temperature and conductivity sensors, two airfoil probes, an optical backscatter sensor, and an altimeter to monitor the instrument approach to the bottom. The airfoils measure high-frequency velocity fluctuations that can be used to estimate the local rate of turbulent dissipation ε (Oakey 1982; Wesson and Gregg 1994). Dissipation data are unreliable in the top 5–10 m owing to contamination by the ship's wake. In stratified water, diapycnal diffusivity was calculated using an assumed relationship with turbulent dissipation and stratification, $K_p \approx 0.2\varepsilon/N^2$ (Osborn 1980).

c. Velocity

We obtained continuous time series of velocity at 1-min intervals and 4-m vertical spacing between 12- and 52-m depths from a 150-kHz broadband shipboard acoustic Doppler profiler (ADCP). Gaps in shipboard data were filled with moored measurements [courtesy of T. Dickey, University of California, Santa Barbara]. Mooring data are presented for visual continuity only; all direct comparisons of shear and turbulent dissipation are made solely with shipboard ADCP data. We calculate barotropic (depth mean) and baroclinic (depth mean removed) velocities as well as shear (first-differenced velocity). Further details of velocity and shear analysis are described in MG05.

3. Observations

a. Meteorological input

Surface heating and wind stress were both strong influences on evolving water properties. The average surface heat flux (J_Q) was -211 W m^{-2} , where the negative sign indicates a net transfer of heat into the ocean (Fig. 1a). The corresponding average buoyancy flux,

$$J_B = \frac{g}{\rho} \frac{\alpha}{c_p} J_Q,$$

was $-6.8 \times 10^{-8} \text{ W kg}^{-1}$, where α is the thermal expansion coefficient and c_p is the specific heat of water (Lombardo and Gregg 1989). Surface heat input was greatly reduced during the passage of storms on year-days 117, 123, 125, and 129. At night heat flux was generally out of the ocean, occasionally rising above 150 W m^{-2} (Fig. 1a, year-days 126, 127). The rain gauge on the WHOI mooring recorded a total of 20.5 mm of rainfall over the fortnight (Fig. 1a).

Three periods of strong wind stress associated with passing storms were separated by calm stretches (Fig. 1b). The average wind stress was 0.08 N m^{-2} . The first storm on year-day 117 lasted only 12 h but contained the strongest wind stresses observed (over 0.4 N m^{-2}). The storm peaked during daytime, neatly but perhaps unfortunately coinciding with the break between microstructure profiling periods. Winds were also elevated in two moderate bursts between year-days 120 and 124. During most of this period we were in port. Last, there was a lower but more sustained period of wind stress lasting from year-days 125 to 129. Wind stress measurements from a moored platform reveal these windy periods to be part of a long series of winter storms that were slowly, but not steadily, declining in magnitude as spring progressed (Chang and Dickey 2001).

b. Water properties: Spring warming

Mid-Atlantic Bight water is part of a “continuous but leaky” large-scale buoyancy-driven shelf current that flows southward from Labrador to Cape Hatteras (Loder et al. 1998). Overviews of the seasonal cycle of stratification and springtime hydrography for this area can be found in Chang and Dickey (2001), Gardner et al. (2001), and Lentz et al. (2003). To first-order, shelf water is stratified from late spring to early autumn and is well mixed during the winter. During the spring portion of the CMO experiment, the water column was characterized by a tall bottom mixed layer (averaging 25 m with a standard deviation of 4 m), a moderate but variable surface mixed layer ($14 \pm 6 \text{ m}$), and growing stratification in between (Fig. 2b). The surface (bottom) mixed layer is defined to include water with a density within 0.01 kg m^{-3} of the lowest (highest) measured density [consistent with Gardner et al. (2001)].

The relative contributions of temperature T and salinity S to growing vertical density gradients can be seen in a daily series of temperature–salinity plots (Fig. 3) or quantified by spice gradients (Fig. 1e),

$$\frac{dV}{dz} \equiv -\alpha\rho \frac{\partial T}{\partial z} - \beta\rho \frac{\partial S}{\partial z}, \quad (1)$$

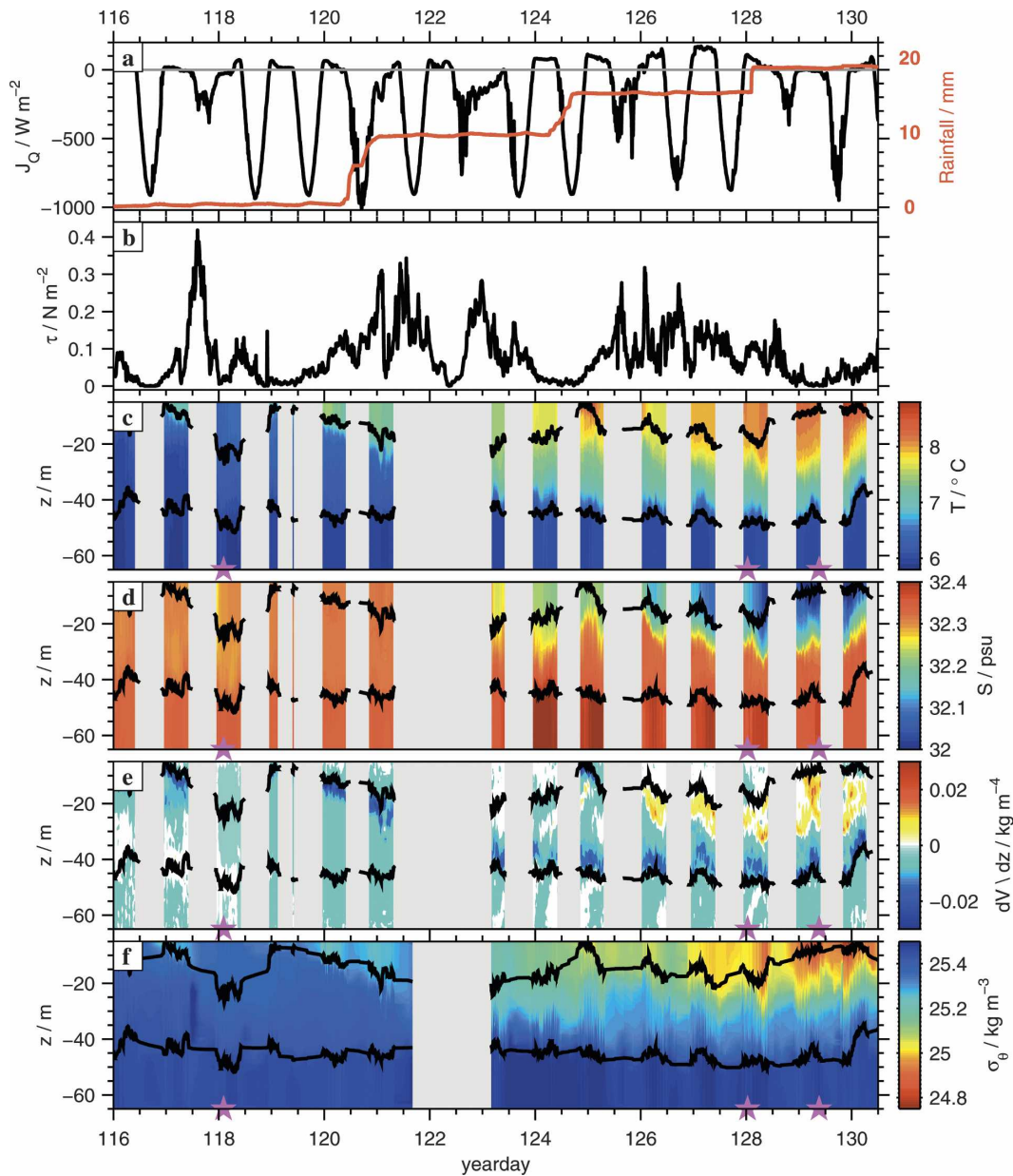


FIG. 1. (a) Surface heat flux (black, left axis, zero line in gray; negative is into the ocean) and rainfall (red, right axis) from WHOI mooring gauge, (b) wind stress, (c) temperature during microstructure profiling periods, (d) salinity during the same periods, (e) spice (see text), and (f) potential density, supplemented by CTD data. In (c)–(f) the boundaries of surface and bottom mixed layers are indicated. The magenta stars indicate the times of the three sample profiles shown in Fig. 5.

where α and β are the thermal and haline expansion coefficients (Veronis 1972). From yeardays 116 to 121, density gradients were almost exclusively due to temperature, indicated by blue patches in Fig. 1e and near-vertical T – S data spread (Fig. 3). During this period, surface temperature gradually rose from 6° to 9°C, while salinity changed little. Warm surface water (from daytime surface heating) was present at the start of

each profiling period (Fig. 3, red dots). Over the course of the night, this water gradually cooled and mixed with underlying water. Following the strong turbulence associated with the storm during the later half of yearday 117 (Fig. 2e), the range of T – S properties was greatly reduced. Lentz et al. (2003) argue that westward wind bursts (such as this storm) are particularly conducive to mixing since associated onshore Ekman transports ad-

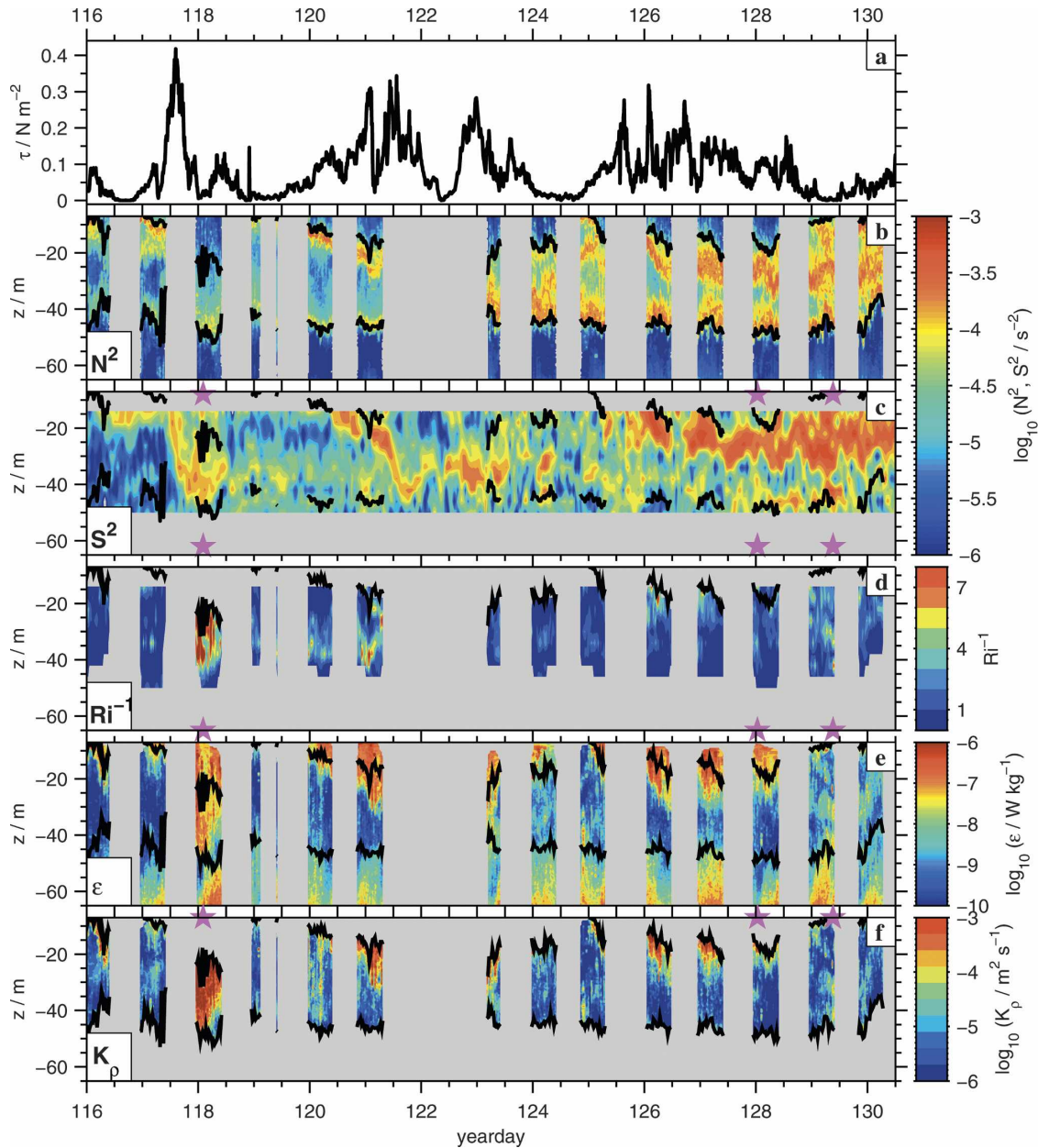


FIG. 2. (a) Surface wind stress (repeated from Fig. 1 for convenience), (b) buoyancy frequency, (c) shear variance from shipboard ADCP data, supplemented with University of California, Santa Barbara, mooring measurements during year-days 121–123 (courtesy of T. Dickey), (d) inverse 4-m Richardson number, (e) turbulent dissipation rate, and (f) diapycnal diffusivity in stratified water. In (b)–(f) the boundaries of surface and bottom mixed layers are indicated. The magenta stars indicate the times of the three sample profiles shown in Fig. 5.

vect cross-shelf density gradients in such a way as to reduce local stratification.

Starting yearday 123, near-surface salinity began to decrease, dropping from 32.25 to 31.9 psu by yearday 129 before rising back up to 32.15 psu on yearday 131. From yearday 126 onward, the salinity of near-surface water showed daily fluctuations with an overall freshening trend (Figs. 1d, 3). During this week deep density

gradients were still due primarily to temperature, but stratification in the upper thermocline was increasingly salinity driven (Fig. 1e, red patches). Temperature and salinity properties in the bottom mixed layer remained remarkably constant during the entire period, suggesting that surface buoyancy forcing did not penetrate below 40-m.

Numerous previous studies have indicated that salin-

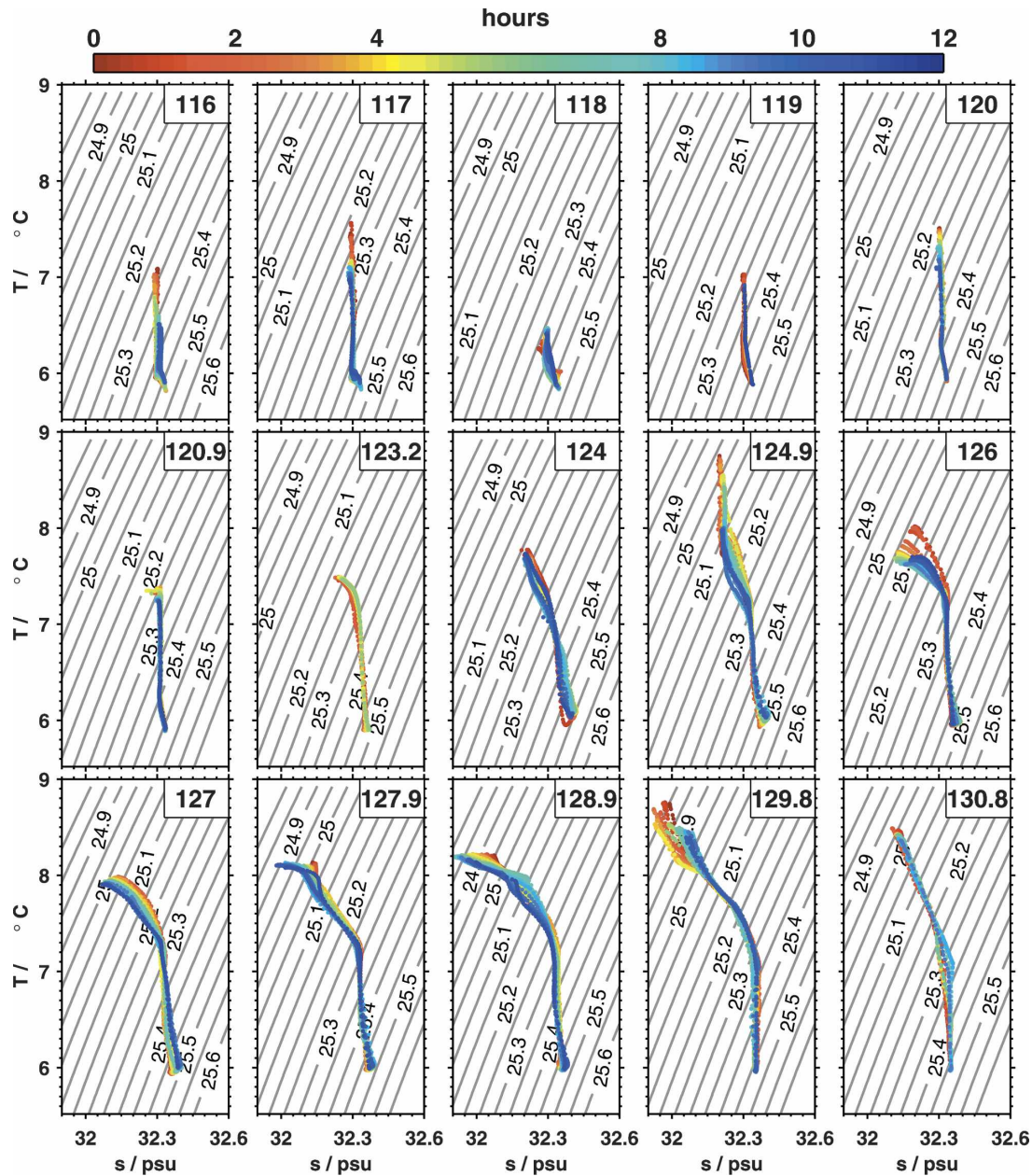


FIG. 3. Temperature and salinity evolution during periods of microstructure observations. The upper-right-boxed number in each panel is the time (yearday) when measurements commenced. Potential density contours are shown in gray. For each panel, the colored dots represent temperature and salinity averaged over 0.5 m and 0.5 h. The color indicates the time of each average, measured in hours from the start of that profiling period (top color bar). The axes range is the same in each panel.

ity is controlled by advection of upstream freshwater sources, from glacial (Greenland, Hudson Bay) and river runoff, while water temperature is set by local surface heating (Chapman and Beardsley 1989; Linder and Gawarkiewicz 1998; Loder et al. 1998; Lentz et al. 2003). The observed temperature rise was consistent in magnitude with local surface heating, especially during

the first week. The depth-integrated heat content of the water column (J m^{-2}) is given by

$$\text{heat} = \int_{-H}^0 \rho c_p T(z) dz, \quad (2)$$

where H is the total water depth (70 m). To test the applicability of one-dimensional heat budgets (in which

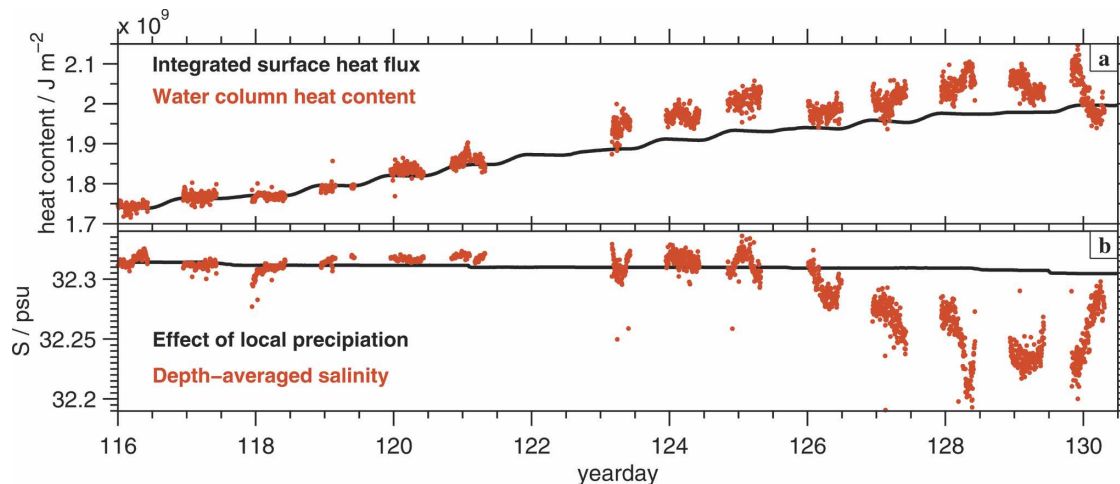


FIG. 4. (a) Integrated surface heat flux (black), cf. Fig. 1a, and depth-integrated water column heat content, (2) (red dots). (b) Observed depth-averaged salinity (red) and depth-averaged salinity expected based on local precipitation (black).

heat content is solely influenced by surface fluxes), we compare the calculated heat content (2) and cumulative integral of surface heat flux (Fig. 4). The two quantities are closely matched through yearday 121. There was a jump in water column heat content between yearday 121 and 123, although rises in heat content both before and after this interlude were consistent in magnitude with integrated surface flux. The increased freshening of the upper water column over the second week was more substantial than could be explained by local rainfall (Fig. 4b). Although the historical average current is westward at this location, Lentz et al. (2003) argue that several periods of near-surface freshening during the spring of 1997 were due to anomalously eastward wind stresses advecting Connecticut River runoff offshore.

As top-to-bottom gradients of salinity and temperature grew, average stratification tripled in magnitude (Fig. 2b). Initially, the strongest density gradients were at the base of the mixed layer. After the passage of the strong storm on yearday 118, near-surface buoyancy was mixed downward, pushing density gradients to the region just above the bottom mixed layer, near 40-m depth. This deep stratification persisted for the next several days as the surface mixed layer and bordering density jump were reestablished. Although we were not present during the storm on yearday 121–123, upon our return surface temperature and salinity gradients had again been mixed to 40-m depth, and the stratification above the bottom mixed layer had strengthened. Over the following week, a stratified layer developed anew immediately below a surface mixed layer and facilitated

the initiation of a spring phytoplankton bloom (Sosik et al. 2001). This layer of near-surface stratification thickened until it merged with the stratified region above the bottom mixed layer, producing a range of continuous density gradients between 10 and 45 m. We will discuss the relationship between evolving stratification, T - S changes, and mixing in section 5.

c. Internal waves

The internal wave climate is described in detail in MG05; here we briefly recapitulate a few relevant results. They found that shear variance from low-mode near-inertial waves grew in response to passing storms. Waves generated during the yearday-118 storm had a mode-1 vertical structure and lasted only about one inertial period (MG05's Fig. 2). Associated shear was concentrated near 40-m depth in the region of strongest stratification (Fig. 2c). They showed that the peak shear during this period produced Richardson numbers below $1/4$, usually taken as a threshold for shear instability. Mode-1 waves also appeared after the yearday-121–123 storm, lasting this time for several inertial periods. Waves appearing during the more sustained wind stress on yeardays 125–129 had a substantially larger component of the second baroclinic mode and lasted through the end of observations on yearday 131. Shear from these mode-2 waves was stronger and more distributed in the water column (Fig. 2c, yeardays 126–130). MG05 argue that the rise of the second baroclinic mode was due in part to changes in stratification and in part to nonlinear transfers of energy between modes through quadratic bottom drag. Shearman (2005) ar-

gues that wave reflections off the coast also play a significant role in setting the baroclinic structure.

d. Turbulence

In this section, we present observations of the turbulent dissipation rate with twofold goals. The first goal is to understand the magnitude, range, and forcing mechanisms of the strongest subsurface buoyancy fluxes (produced by turbulence in stratified water); we will show that the strongest mixing was in the entrainment zone at the base of the surface mixed layer except during times of strong internal wave shear or weak winds. The magnitude and patterns of turbulent buoyancy fluxes will then be related to the patterns of spring restratification in section 5.

The second goal is to investigate the magnitude of turbulence away from mixed layer entrainment zones, which we will refer to as midcolumn turbulence (hereinafter defined as data above the bottom mixed layer and more than 5 m below the base of the surface mixed layer). Associated midcolumn mixing is rarely as strong as that at the mixed layer base, but may be an important control of turbulent nutrient transport from deeper waters. We will show that there is significant correlation between turbulence and internal wave shear, though the nature of that relationship fundamentally shifts when the Richardson number from the lowest-mode internal waves is subcritical. The quantitative relation between midcolumn turbulence and shear will be evaluated in light of several candidate turbulence parameterizations in section 4.

Based on expected differences in forcing dynamics, turbulence observations are subdivided into three subsections below: turbulence near the surface, in a bottom mixed layer, and in the stratified region in between.

1) SURFACE-FORCED TURBULENCE

Surface forcing produced the most active turbulence in stratified water, though its range was confined to within 10 m below the surface mixed layer base (Fig. 2). The strongest dissipation rates within the surface mixed layer were observed on yeardays 121, 126, and 127 coincident with periods of strong wind. The average dissipation rate in the observed portion of the mixed layer was $1.9 \times 10^{-7} \text{ W kg}^{-1}$. The average diffusivity and downward buoyancy flux (assuming a mixing efficiency of 0.2) at the mixed layer base were $3 \times 10^{-4} \text{ m}^2 \text{ s}^{-1}$ and $4 \times 10^{-8} \text{ W kg}^{-1}$, respectively.

Based upon similarity scaling and previous oceanic measurements, we expect surface mixed layer turbulence to be a sum (W kg^{-1}) of that produced by wind stress and that by convection (Lombardo and Gregg 1989),

$$\varepsilon_{\text{surf}} = C_1 \varepsilon_{\text{wind}} + C_2 \varepsilon_{\text{convect}},$$

$$\varepsilon_{\text{wind}} = \frac{u_*^3}{kz} = \frac{1}{kz} \sqrt{\frac{\tau_w}{\rho_0}}^{3/2}, \quad \text{and}$$

$$\varepsilon_{\text{convect}} = J_B(z = 0), \quad (3)$$

where $k = 0.4$ is von Kármán's constant, and C_1 and C_2 are proportionality constants. Lombardo and Gregg (1989) find that using $C_1 = 1.76$ and $C_2 = 0.58$ produces a reliable estimate of average dissipation rate throughout the mixed layer. The average mixed layer dissipation rate based on (3) was $2.1 \times 10^{-7} \text{ W kg}^{-1}$, where (3) was evaluated only for the depth range of reliable data. This range does not include locations within 5 m of the surface, where surface wave breaking may be important. Convectively driven turbulence ($\varepsilon_{\text{convect}}$) was comparable to wind stress in its effect on turbulence only on one night, yearday 127. The dissipation rate calculated from (3) during three example periods is shown in Fig. 5 (cyan).

To evaluate the relative roles of wind stress and internal wave shear on dissipation below the mixed layer, we compute correlation coefficients between the dissipation rate at different depths and either surface wind stress or baroclinic energy at 12 m (a simple metric of internal wave strength). To compare quantities at a similar depth below the mixed layer base, we compute averages in a frame of reference moving with the mixed layer depth. The average correlation coefficients are shown as functions of depth below the mixed layer in Fig. 6a. The dissipation rate was most strongly correlated with wind stress from the surface to 5–8 m below the mixed layer depth. Below the mixed layer entrainment zone, the dissipation rate was more significantly correlated with internal wave energy than wind stress (Fig. 6a).

2) BOTTOM-FORCED TURBULENCE

The average dissipation rate in the bottom mixed layer ($3.3 \times 10^{-8} \text{ W kg}^{-1}$) was an order of magnitude weaker than the surface rate (Fig. 2e). Both the magnitude of turbulent dissipation and the correlation between dissipation rate and bottom stress declined steadily with increasing height above the bottom mixed layer cap (Fig. 7a). The law-of-the-wall scaling predicts the dissipation rate (W kg^{-1}) to decrease above the bottom as

$$\varepsilon = \frac{C_D^{3/2} U_{52}^3}{kz_{\text{mab}}}, \quad (4)$$

where k is von Kármán's coefficient (0.4) and z_{mab} is the distance above bottom. MG05 compared microstructure measurements taken within 2 m of the bottom

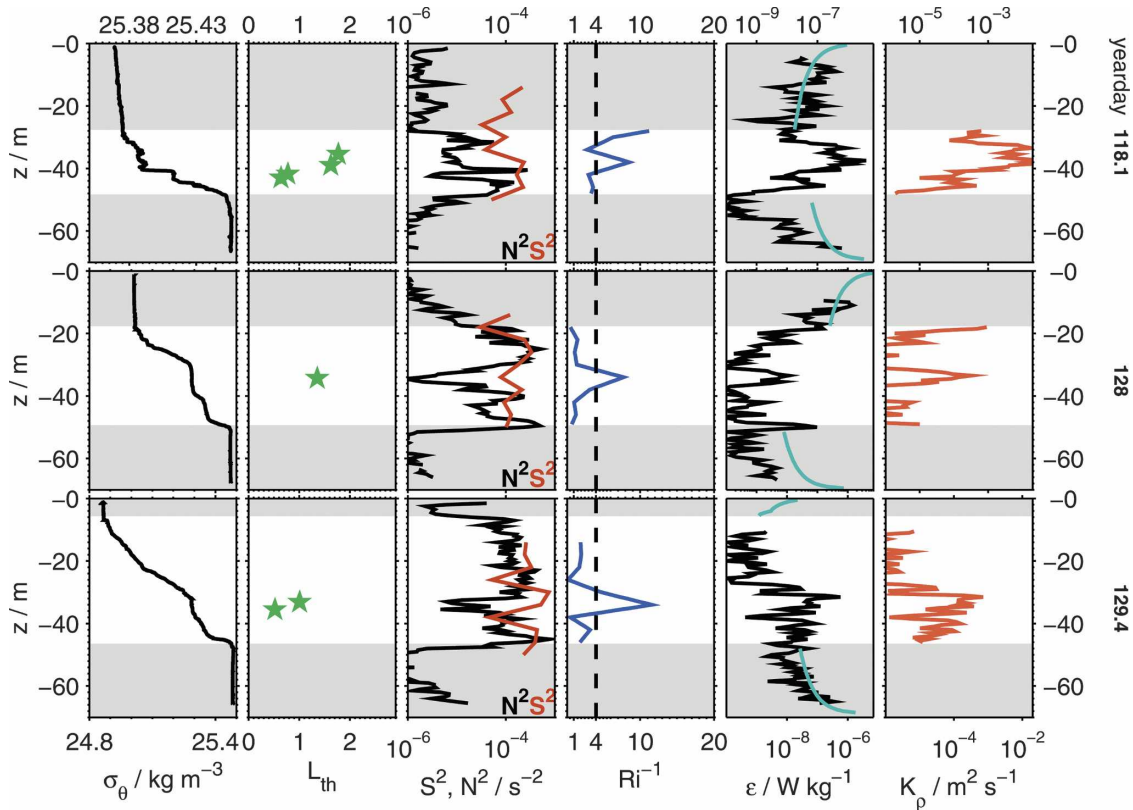


FIG. 5. From top to bottom, three sets of profiles, from year days 118.09, 128.03, and 129.38 (times are also indicated in Figs. 1 and 2). For each time period, quantities plotted are (from left to right) potential density, Thorpe scale, shear variance (red) and stratification (black), inverse Richardson number, observed turbulent dissipation rate (black) and modeled frictional surface (3) and bottom boundary layer (4) dissipation rates (cyan), and diapycnal diffusivity. (top) Potential density during the first period is plotted with a smaller range for clarity; (bottom) the range for the middle and bottom density plots is given. All other quantities are plotted with the same axes limits for the three time periods. The shaded areas in each panel show the extent of the surface and bottom mixed layers.

with current speed at the deepest ADCP bin (52 m) and calculated a drag coefficient of $C_D = 10^{-3}$ based on the method of Dewey and Crawford (1988). This estimate of boundary layer dissipation agrees with observations up to 20 m above the bottom when an actively turbulent boundary layer is well established (Fig. 5, bottom panel), but overestimates dissipation in the upper reaches of the bottom mixed layer when boundary layer turbulence is weak or growing (Fig. 5, top and middle panels, cf. Fig. 2). At the top of the bottom mixed layer (on average 25 m above bottom) the average dissipation rate and diffusivity were weak (Fig. 7c). Dissipation in this stratified mixed layer cap was more correlated with internal wave shear than bottom stress (Fig. 7a, year days 124 and 129 in Fig. 2).

3) MIDCOLUMN TURBULENCE

Dissipation away from boundary layers was initially very weak near or at the instrumental noise level of

$10^{-10} \text{ W kg}^{-1}$ (Fig. 2). Subsequent periods of increased midcolumn dissipation followed patches of elevated shear and stratification, for example, on year day 118 (between 30 and 40 m), 123 (30–40 m), and 129 and 130 (25–35 m) (Fig. 2). Some periods of strong dissipation, such as near 20 m on year day 126, coincided both with strong mixed layer turbulence and strong sub-mixed-layer internal wave shear.

To understand the changing patterns of midcolumn turbulence, we now look in detail at profiles of various quantities taken during three periods that illustrate the range of observed data properties: strong turbulence in weak stratification (year day 118), weak turbulence in developed stratification (year day 128), and moderate turbulence in developed stratification (year day 129).

On year day 118, turbulence and diffusivity were elevated over a 15–20-m patch between surface and bottom mixed layers (Fig. 5, top row). Shear during this period was from a first-mode near-inertial wave (MG05). Shear variance was larger than the stratifica-

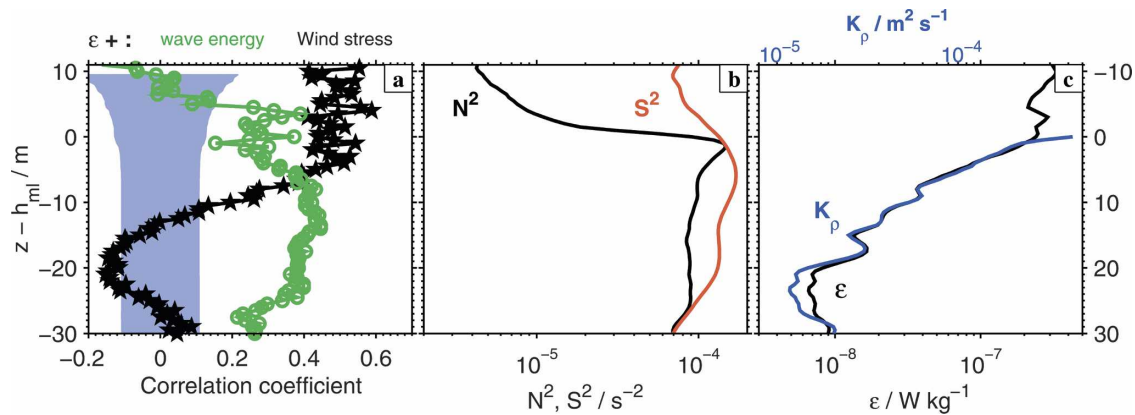


FIG. 6. (a) Correlation coefficient between dissipation and wind stress (black stars) in a frame of reference moving with the base of the surface mixed layer and correlation between dissipation and baroclinic energy (green circles); the shaded area indicates significance. (b) Shear variance and stratification and (c) turbulent dissipation rate (black, bottom axis) and diapycnal diffusivity (blue, top axis), both averaged in the same moving frame of reference.

tion over most of the water column, pushing the inverse Richardson number above 4, which is usually taken as the threshold for shear instability (for convenience we will refer to this as an unstable Richardson number, or unstable shear). There were clear overturns in the density profile, with Thorpe scales (Ivey and Imberger 1991) of 0.5–2 m (Fig. 5, top row, second panel from left) and overturn sizes of twice that (not shown). Instrument resolution prevents observations of overturns less than 0.5 m tall. Diapycnal diffusivity was over three orders of magnitude larger than open-ocean background values of $5 \times 10^{-6} \text{ m}^2 \text{ s}^{-1}$ (Gregg 1989) and mirrored the depth structure of dissipation rate (Fig. 5, top right panel).

The second set of profiles (yearday 128, Fig. 5 middle

panels) was from a time of weak midcolumn turbulence except for one overturning event. Shear was from a mode-2 wave (MG05) and was more evenly distributed between surface and bottom mixed layer boundaries. Stratification was significantly stronger than on yearday 118. The inverse Richardson number rose above critical in a patch of weakly stratified water. A single density overturn was observed coincident with the unstable Richardson number, with a patch height of 4.2 m and a Thorpe scale of 1.35 m. Dissipation was elevated in this patch as well as in an entrainment zone at the base of the surface mixed layer and in a small patch at the top of the bottom mixed layer. Diffusivity again mirrored dissipation and was elevated an order of magnitude above background levels in the overturning patch.

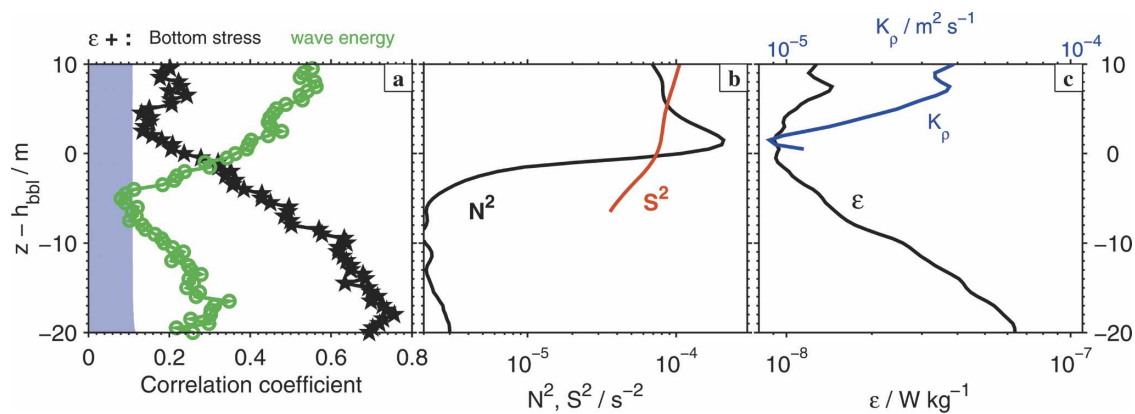


FIG. 7. (a) Correlation coefficient between dissipation and bottom drag (black stars) in a frame of reference moving with the top of the bottom mixed layer and correlation between dissipation and baroclinic energy (green circles); the shaded area indicates significance. (b) Shear variance and stratification and (c) turbulent dissipation rate (black, bottom axis) and diapycnal diffusivity (blue, top axis), both averaged in the same moving frame of reference.

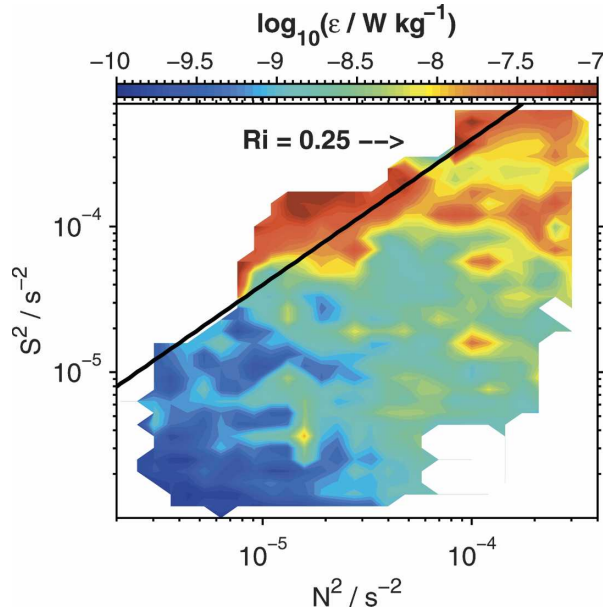


FIG. 8. Midcolumn dissipation averaged in logarithmically evenly spaced bins of shear and stratification. Data within the surface and bottom mixed layers or within 5 m below the base of the surface mixed layer are excluded. The $Ri = 1/4$ line is contoured for reference.

The final set of profiles (Fig. 5, bottom panels, year-day 129.38) was from a time of moderate midcolumn turbulence. The stronger midcolumn shear reflected the presence of energetic, higher-mode near-inertial waves (MG05). The inverse Richardson number was well above critical in a patch that coincided with the largest shear. Dissipation was elevated in and below the supercritical shear. Two overturns were present, with Thorpe scales of 0.5 and 1 m, and patch scales twice that size. Diffusivity was near $10^{-4} \text{ m}^2 \text{ s}^{-1}$ over a 20-m range above the bottom mixed layer.

More systematically, the relationships between shear,

stratification, and midcolumn dissipation can be seen by bin averaging dissipation (Fig. 8). Consistent with our qualitative observations, the strongest dissipation occurred during patches of unstable Richardson number (to the left of the black $Ri = 0.25$ line). These data are primarily from yearday 118, though there were also periods near the end of the record when strong mode-2 shear produced near-critical Richardson numbers (MG05). On the stable (right) side of the $Ri = 0.25$ line, bin-averaged dissipation rates increase with both increasing shear and increasing stratification (from bottom left to top right). This pattern suggests a dynamic link between low-mode shear and dissipation even when the low-mode shear is stable. The relationship between shear, stratification, and dissipation will be further explored in section 4.

e. Summary of changes during spring restratification

There were substantial changes in the strength of stratification, shear, and patterns of turbulence during spring restratification. These changes are epitomized by average profiles over yearday 118 (which dominated the first week) and yeardays 128–130 (Fig. 9). During yearday 118 (thin, black), stratification was present but weak, and shear variance from moderately strong mode-1 near-inertial waves was more than 4 times the average stratification. Elevated dissipation rates extended 50 m below the surface, reflecting both the large mixed layer depth (over 30 m early in the night) and active turbulence below the mixed layer coincident with unstable Richardson numbers from internal wave shear (Fig. 5). Diffusivity was several orders of magnitude above background levels, reflecting both elevated dissipation and low stratification. After yearday 128 (Fig. 5 and Fig. 9, thick, gray line) the water column was

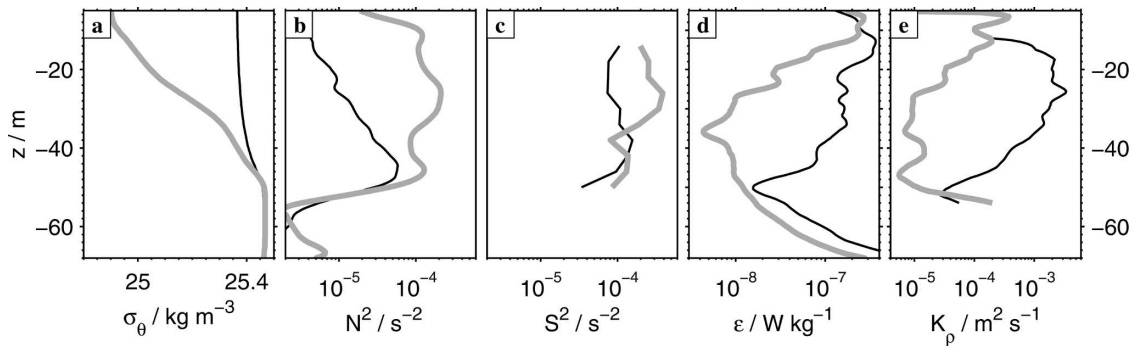


FIG. 9. Average profiles of various properties from two periods representative of the first week (yearday 118, thin black) and the second week (yeardays 128–130, thick gray) of observations: (a) potential density, (b) buoyancy frequency, (c) shear variance (with the same axes range as N^2 for comparison), (d) turbulent dissipation rate, and (e) diapycnal diffusivity (defined only away from well-mixed surface and bottom layers).

significantly more stratified and wave shear was, on average, less than 4 times stratification. The average dissipation rate and diffusivity were comparable to open-ocean thermocline values in magnitude: both diminished with increasing depth below the surface mixed layer, then rose again in a deeper stratified region approaching the bottom mixed layer cap.

4. Parameterizing turbulence

In this section we evaluate several candidates for parameterizing the turbulent dissipation rate in terms of more easily observed or modeled quantities, such as stratification and shear. There are numerous turbulence parameterizations in the literature that relate turbulent dissipation, shear variance, and stratification; these formulas are partly empirical and partly based upon kinematic or dynamic models. Parameterizations can be differentiated by their implicit dynamics, the scales of motion that need to be resolved, and the degree of averaging required. We consider two classes of turbulence models below. Figure 10 shows profiles of inverse Richardson number and observed turbulent dissipation averaged for 45 min surrounding the times of the snapshots of Fig. 5; the parameterizations described below will be compared with these average profiles.

a. Dimensional scalings of turbulence

There is a large body of work that diagnoses turbulent dissipation as the ratio of available energy and a characteristic time scale of the turbulence, irrespective of the large-scale dynamics that may generate instabilities. The simplest scalings take characteristic energy and time scales from observations of the largest stratification-limited eddies. In particular, with eddy size given by measured Thorpe scales and an eddy overturning time set by stratification, dissipation (W kg^{-1}) can be estimated as (Dillon 1982; Ivey and Imberger 1991; Mowm 1996; Baumert and Peters 2000)

$$\varepsilon_{\text{Th}} = L_{\text{Th}}^2 N_{\text{ot}}^3, \quad (5)$$

where N_{ot} is the average stratification within an overturn based upon resorted density profiles. Application is limited by the resolution of density overturning length scales. When overturns are observed, the dissipation rates estimated from (5) are roughly the same magnitude as the rates calculated from microstructure (Fig. 10, green stars). However, the scatter is large and there is a tendency for underestimation when the turbulence is very active (Fig. 10, top) and overestimation in weaker turbulence (Fig. 10, middle, bottom).

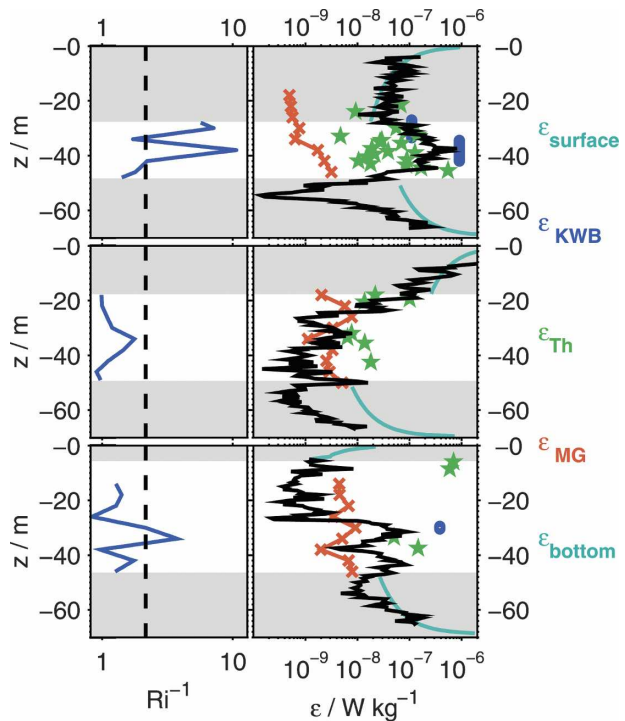


FIG. 10. (left) Inverse Richardson numbers averaged over approximately 45 min surrounding the times of snapshot profiles shown in Fig. 5; (right) dissipation averaged over the same periods. For each time period, the model dissipation rates based on the summer CMO MacKinnon–Gregg parameterization (red), the KWB parameterization (blue), and Thorpe-scale estimates (green) are also shown. Estimates of surface and bottom boundary layer turbulence (cyan) are reproduced from Fig. 5.

A more sophisticated dimensional turbulence scaling is proposed by Kunze et al. (1990) (hereinafter referred to as KWB) and explored by Polzin (1996). The dissipation rate (W kg^{-1}) is taken as the ratio of the kinetic energy loss needed to return the Richardson number to 0.25 and a characteristic time scale for shear instability,

$$\varepsilon_{\text{KWB}} = (\Delta z)^2 \left\langle \left(\frac{S^2 - 4N^2}{24} \right) \left(\frac{S - 2N}{4} \right) \right\rangle, \quad (6)$$

where Δz is the depth range over which $\text{Ri} < 1/4$, and velocity and density are differenced over this depth range to calculate S and N . The model is meant to characterize the dissipation rate averaged over the lifetime of a turbulent event. Application is ideally based upon shear and stratification profiles right before instability begins, although in practice measurements are taken throughout an instability event. The advantage over a simpler Thorpe-scale estimate is that this method can be potentially used in models that accurately reproduce unstable wave shear but do not explicitly resolve static instabilities.

Comparison of (6) with observations is limited to measurements that resolve unstable Richardson numbers; for our data, this criterion is met only when the lowest-mode waves are unstable (section 3d). Dissipation estimated with this method agrees well with the strong turbulence observed during instabilities on year-day 118 but overestimates turbulence on year-day 129 when the average Richardson number is marginally unstable (Fig. 10, blue dots).

b. Wave–wave interaction parameterizations of turbulence

Wave–wave interaction parameterizations (Heney et al. 1986, hereinafter HWF; Polzin et al. 1995; Sun and Kunze 1999; MGb) assume that the energy-containing waves (which MG05 define to include the first four vertical modes on the shelf) are stable (in a Richardson number sense), the wave instabilities that lead to turbulence happen on a scale below measurement resolution, and the rate of turbulent dissipation is controlled by wave–wave interactions that transfer energy from large- to small-scale motions. These models are meant to represent bulk averages of turbulent properties, not to reproduce individual wave-breaking events. Within this category, models are differentiated by the assumptions about the statistical nature of the wave field and the interactions among waves.

Here we again consider the low-mode energy-containing waves to be the first four modes, those reliably resolved by the shipboard ADCP (MG05). The observations fall into two dynamical categories: cases in which the low modes produce subcritical Richardson numbers (e.g., year-day 118) and cases in which the lowest modes are stable (most of the time after year-day 126). Wave–wave interaction models may characterize the rate of turbulent dissipation in the later case; we would not expect models based on wave–wave interaction to be appropriate in the former case.

One of the most enduring wave–wave interaction models is the eikonal model of HWF, which has been successfully compared with numerical simulations, and, with slight modification, with ocean microstructure by Gregg (1989) and Polzin et al. (1995). The model is based on the fate of small-scale waves propagating through velocity gradients from much larger waves. The vertical scales of some small waves (“test waves” in HWF) shrink as they refract in the shear field until they become susceptible to instability and break. The rate of turbulent dissipation is related to the rate of spectral energy transfer through assumptions about the statistically steady-state spectral properties of the wave field. We will refer to the popular incarnation of this param-

eterization given by Gregg (1989) as the Gregg–Heney scaling (hereinafter ε_{GH} ; W kg^{-1}); it is given by

$$\varepsilon_{\text{GH}} = 1.8 \times 10^{-6} \left[f \cosh^{-1} \left(\frac{N_0}{f} \right) \right] \left(\frac{S_{10}^4}{S_{\text{GM}}^4} \right) \left(\frac{N^2}{N_0^2} \right), \quad (7)$$

where

$$S_{\text{GM}}^4 = 1.66 \times 10^{-10} \left(\frac{N^2}{N_0^2} \right)^2 (\text{s}^{-2}), \quad (8)$$

S_{10} is the measured 10-m shear, f is the Coriolis frequency, and $N_0 = 3$ cph.

The Gregg–Heney scaling fails to reproduce the kinematic relationships observed here. Figure 11 (top row) shows only the $\text{Ri} > 1/4$ portion of our bin-averaged dissipation data (cf. to Fig. 8), the equivalent plot based upon (7), and a scatterplot of one against the other. The ε_{GH} relationship has too strong a dependence on shear (going top to bottom in the bin-averaged dissipation plots): ε_{GH} also varies inversely with stratification for a given level of shear. However, the observed dissipation increases with both shear and stratification. The correlation between $\log(\varepsilon)$ and $\log(\varepsilon_{\text{GH}})$ is only 0.5 (Fig. 11, upper right).

In contrast, MGa proposed an alternate interpretation of the original HWF model. They argue that in a wave field in which there is no statistical relationship between shear in low- and high-mode waves (MGb) the strength of low-mode (background) shear is decoupled from properties of high-mode test waves. The rate of spectral energy transfer, and hence the dissipation rate (W kg^{-1}), then scales as

$$\varepsilon_{\text{MG}} = \varepsilon_0 \left(\frac{N}{N_0} \right) \left(\frac{S_{\text{lf}}}{S_0} \right), \quad (9)$$

where S_{lf} is the low-frequency, low-mode resolved shear, $S_0 = N_0 = 3$ cph. The best fit to data is achieved with $\varepsilon_0 = 1.1 \times 10^{-9}$. Note this is larger than the ε_0 value used by MGa, for unknown reasons. However, the functional $\varepsilon(S, N)$ scaling is the same for both datasets. The MGa model dissipation rate displays a similar range of magnitudes and the same pattern as the observed data (Fig. 11, bottom middle). The correlation coefficient between $\log(\varepsilon)$ and $\log(\varepsilon_{\text{MG}})$ is 0.85 (Fig. 11, bottom right). This parameterization is compared with the averaged dissipation profiles in Fig. 10 (right column, red). Of the three examples, the model dissipation (ε_{MG}) fares best against observed data during the beginning of year-day 128 (middle). While the individual profile shown in Fig. 5 had unstable shear, the average inverse Richardson number for this period was less than 4.

Dissipation during times when the lowest modes

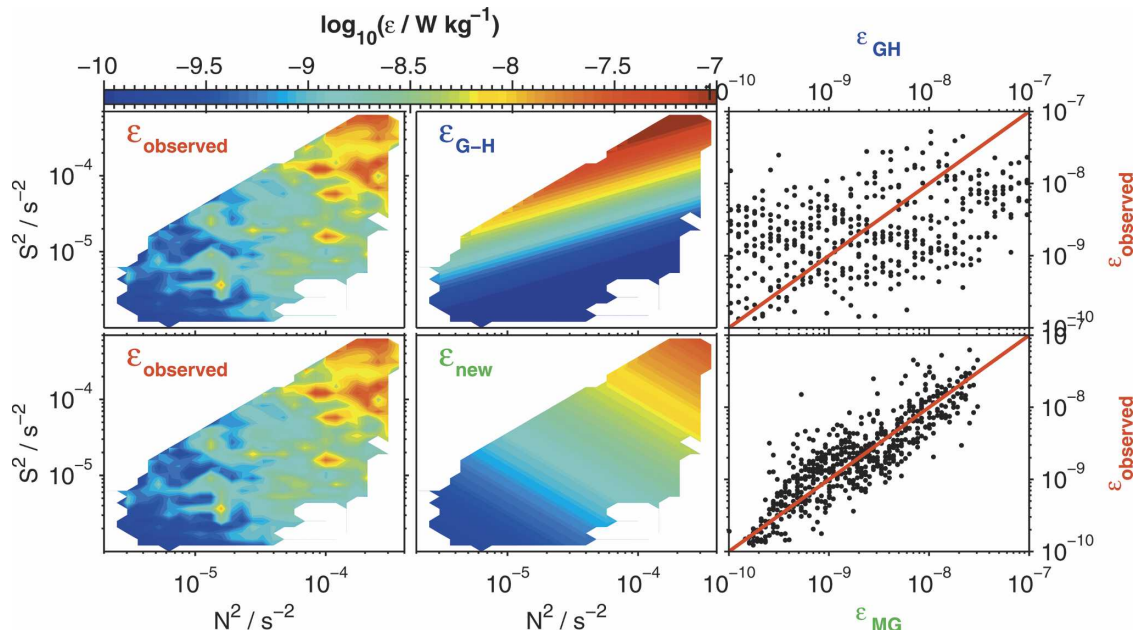


FIG. 11. (left) Dissipation binned in logarithmically evenly spaced bins of stratification (x axis) and shear variance (y axis). Only data with $Ri > 1/4$ are shown. (middle) Similar bin-averaged dissipation based upon (top) (7) and (bottom) (9). (right) Observed dissipation plotted against modeled (top) ϵ_{GH} and (bottom) ϵ_{MG} dissipation.

were unstable is poorly captured by parameterizations based on wave–wave interaction. Modeled dissipation (ϵ_{MG}) is several orders of magnitude too low during the period of subcritical Richardson numbers on yearday 118 and a factor of 10 too small in the deeper portion of midcolumn dissipation on late yearday 129 (Figs. 10a,c). During such periods the dissipation rate is poorly correlated with both ϵ_{GH} and ϵ_{MG} (correlation coefficients of 0.17 and 0.03, respectively). This lack of correlation is not surprising: both models are based on the assumption that the rate-controlling process of turbulence generation is wave–wave interaction. When shear from the lowest modes is unstable, no wave–wave interaction is necessary to produce turbulence, and we should not expect this class of parameterizations to be appropriate.

c. Regime shifts in turbulence parameterizations

Our results suggest two qualitatively different regimes for turbulent dissipation on the shelf. In the first regime, the energy-containing modes, which are directly generated by external forcing (MG05), produce subcritical Richardson numbers due to a combination of wave strength and weak stratification. The resulting turbulence is strong. In the second regime, the energy-containing modes are stable and lead to weaker turbulence through the process of wave–wave interactions. The difference between these regimes may be formally

expressed using the “wave–turbulence” transition theory of D’Asaro and Lien (2000).

Though it is only applicable in a few instances in this dataset owing to low instrument resolution, the KWB scaling provides a useful rubric for thinking about turbulence dissipation as available kinetic energy lost over a characteristic time scale. Consider that, for the two dynamic regimes discussed here (turbulence from instabilities of the lowest modes versus that from smaller test waves propagating in a shear field created by stable low modes), instability in each case occurs when total shear is greater than, but the same order of magnitude as, local stratification. The appropriate time scale of the instability is thus of the same order for both regimes, whether based on a shear instability growth rate, $(S - 2N)/4$, or a turbulent overturning time scale, N . The large difference in dissipation rate must therefore be related to the energy available to turbulence in each case as

- 1) *Regime 1* (energy-containing modes unstable, e.g., yearday 118): the available kinetic energy is based on the (large) energy in low-mode waves. Specifically, the energy that is available depends on the wave strength and thickness of the region over which shear is unstable. The dissipation rate may be locally prescribed by dimensional scalings along the lines of (6), but must ultimately be related to the full complexity of external forcing because it projects

onto local stratification (MG05). The strong resultant dissipation was, in turn, a significant drain on the energy of mode-1 waves (MG05).

- 2) *Regime 2* (energy-containing modes stable, e.g., yearday 128): the available kinetic energy is assumed to be from small-scale propagating test waves that interact with the background shear from low-mode waves. This available energy is significantly lower than available energy in the first regime for two reasons. First, test waves break only when they have become small enough that shear is unstable; hence, Δz in (6) is small. Second, test wave energy is less available because it is more patchy in time. For example, in the second sample period (yearday 128), the snapshot profiles (Fig. 5, middle) show a small-scale instability and elevated turbulence, but unstable Richardson numbers and elevated turbulence do not survive when averaged over 45 min (Fig. 10, middle).

5. Discussion

a. Coastal mixing context

The average turbulent diffusivity was an order of magnitude larger in the spring than in late summer (MGa), though the patterns and kinematic parameterizations of turbulence were consistent across season. Here we have argued that the relationship between midcolumn turbulence and internal wave shear can be divided into two dynamic regimes: one in which the energy-containing modes have subcritical Richardson numbers and produce strong turbulence and one in which the energy-containing modes are stable and lead to weaker turbulence through wave-wave interactions.

We observed examples of the former category in both spring (moderately large near-inertial waves in weak stratification) and summer (solibores). In both cases, calculated diffusivities were near or above $10^{-3} \text{ m}^2 \text{ s}^{-1}$ and turbulent dissipation was strong enough to quickly drain energy from the wave that created it (MGa,b; MG05). We also observed examples of the second category (stable energy-containing waves) in both seasons. Remarkably, though the shear in summer was largely tidal and in the spring was dominantly near inertial, the same kinematic turbulence parameterization applied in both cases (cf. Fig. 11 with MGa's Fig. 13).

These diffusivity estimates are roughly consistent with those of other CMO observations, though all other dedicated mixing measurements were made in the summer only. MGa found their summer turbulence measurements to be consistent with those of Rehmann and Duda (2000) and Ledwell et al. (2004). More generally,

the success of the same parameterization in predicting dissipation from both tidal (summer) and near-inertial (spring) internal waves suggests that the results presented here may be applicable to a wide range of coastal environments.

b. Relative magnitude of turbulent fluxes

The buoyancy flux associated with observed dissipation rates provides an upper bound on the effectiveness of turbulent mixing for downward transport of surface heat. The average surface buoyancy flux from solar heating was $-6.8 \times 10^{-8} \text{ W kg}^{-1}$ (section 3a). Assuming a mixing efficiency of 0.2, a turbulent dissipation rate of $3.4 \times 10^{-7} \text{ W kg}^{-1}$ is required to move buoyancy (heat) downward at the rate it enters the ocean. Observed dissipation rates were this large immediately below the base of the surface mixed layer (Fig. 6), during the strong turbulence on yearday 118 (Figs. 5 and 9), and in the high-shear region extending 10–15 m below the mixed layer base on yeardays 126 and 127 (Fig. 2d). Most of the time, however, the buoyancy flux well below the surface mixed layer was an order of magnitude or more lower than surface fluxes (e.g., Fig. 10b), implying that buoyancy input was primarily stored in the surface mixed layer.

Another estimate of turbulent strength is the dimensional time scale given by

$$t_{\kappa} = \frac{L^2}{K_{\rho}}, \quad (10)$$

where L is a characteristic vertical length scale of scalar gradients (nutrients, heat, pollutants), and t_{κ} is the time over which a diffusivity K_{ρ} can significantly modify those gradients. Consider the representative diffusivity profiles in Figs. 6 and 9e. A diffusivity of $10^{-3} \text{ m}^2 \text{ s}^{-1}$ could, for example, significantly modify a 10-m feature over the course of one day. On the other hand, the late-spring average diffusivity of $10^{-5} \text{ m}^2 \text{ s}^{-1}$ would take months to affect the same size feature. On that time scale, water with an along-isobath mean speed of 0.1 m s^{-1} could reach Cape Hatteras (Chapman and Beardsley 1989; Chang and Dickey 2001)

c. Turbulence and spring restratification

Several previous studies have considered the spring restratification problem as one in which temperature evolution can be modeled as a one-dimensional result of local solar heating (Ou and Houghton 1982; Aikman 1984; Chapman and Gawarkiewicz 1993). The similarity of both evolving heat content versus integrated surface heat flux (Fig. 4) and the magnitude of surface versus turbulent fluxes (section 5b) would support the validity of one-dimensional models for temperature evolution.

However, it remains to be seen whether the particular evolving patterns of heat distribution with depth (Fig. 1) are consistent with local turbulent mixing.

The time series of diffusivity presented here provides an opportunity to explicitly evaluate the appropriateness of one-dimensional mixing assumptions. To address this question we construct a simple thought experiment model of temperature evolution. We start with an initial temperature profile, $T(z, t_0)$, and consider the evolution in time based on two simple rules. First, local surface heat fluxes are “instantaneously” mixed within the surface mixed layer, whose depth (h_{ml}) is taken as the observed values. Concurrent optical measurements show approximately 90% of downward irradiance is trapped in the top 15 m, near the average mixed layer depth (Gardner et al. 2001). Second, temperature below the mixed layer evolves in accordance with observed diffusivity profiles. This model, dubbed model A, is thus given by

$$T_A(z, t + \Delta t) = T_A(z, t) + \frac{J_Q(t)}{h_{ml}(t)\rho c_p} \Delta t,$$

$$\text{for } z \geq -h_{ml}(t)$$

and

$$= T + A(z, t) + \frac{d}{dz} \left[K_{obs}(z, t) \rho_0 \frac{dT_A}{dz} \right] \Delta t,$$

$$\text{for } z < -h_{ml}(t), \quad (11)$$

where $h_{ml}(t)$ and K_{obs} are the evolving mixed layer depth and diffusivity profiles. A background diffusivity of $2 \times 10^{-6} \text{ m}^2 \text{ s}^{-1}$ is used when no diffusivity measurements were available. Both sets of observations were interpolated onto a time grid of $\Delta t = 100 \text{ s}$. A simple central differencing scheme was used to calculate derivatives. Because of the lack of measurements between yearday 121 and 123, and the significant T - S changes during this period, the model was run in each of two time periods: yeardays 116–121 and 123–131. In each case, the model was initialized with an observed temperature profile.

For comparison, a second simpler model (model B) was considered in which all surface heat fluxes are assumed to be trapped in the top 20 m:

$$T_B(z, t + \Delta t) = T_B(z, t) + \frac{J_Q(t)}{h_{ml}\rho c_p} \Delta t, \quad \text{for } z \geq -h_{ml}$$

and

$$= T_B(z, t), \quad \text{for } z < -h_{ml}, \quad (12)$$

where $h_{ml} = 20 \text{ m}$.

Final results for both models, for each of the two time periods, are shown, along with observed initial and final

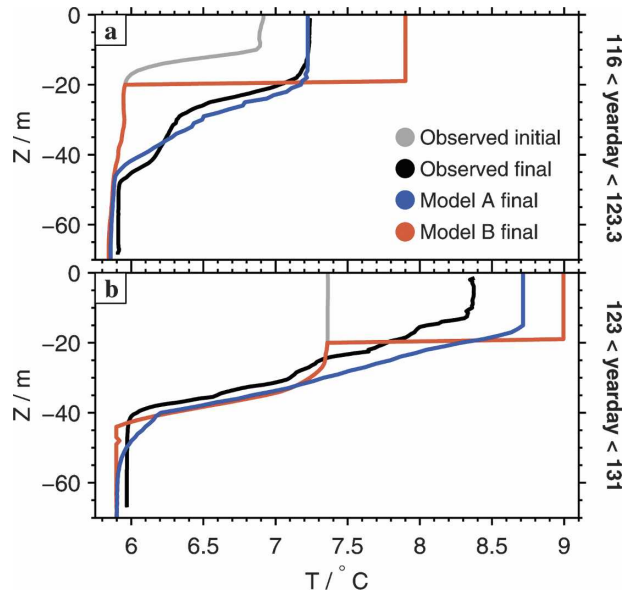


FIG. 12. Initial (gray) and final (black) observed temperature and final modeled temperature from models A and B for the time period (a) between yeardays 116 and 121 and (b) between yeardays 123 and 131.

temperature profiles in Fig. 12. For the first time period (top), the final temperature based on estimated diffusivities (model A, blue) agrees quite well with the observed final temperature profile (black), especially considering that there were no mixing observations during the peak of the yearday 118 storm, when wave-related turbulence may have been at its peak (MG05). During the second week (bottom), the model warms the surface water more than is observed; the discrepancy can be attributed to advection that has brought cooler and fresher water to these depths (Fig. 3, Lentz et al. 2003). In both time periods, model B, which simply mixes incoming heat within a static mixed layer, unrealistically traps heat near to the surface (Fig. 12, red).

Conclusions to this thought experiment are twofold. First, the initial onset of warming-induced spring stratification can be reasonably considered as a one-dimensional mixing process, though near-surface advection becomes important as the spring runoff arrives. Second, the variability of mixed layer entrainment, on daily time scales, is an essential component of downward heat redistribution. The repeated deepening and shoaling of the mixed layer and occasional periods of energetic internal wave-related turbulence combine to pump heat well below the surface, leaving behind a continuous temperature gradient. The larger implication is that models using mixed layer depth or wind stress measurement with less than weekly resolution may overestimate near-surface heating by up to a factor of 2 (Fig. 12).

6. Conclusions

We have analyzed observations of turbulent dissipation and mixing during the spring restratification period on a wide, flat continental shelf. One of the primary goals of turbulence research is to be able to predict the patterns and magnitude of turbulent fluxes (of nutrients, pollutants, dissolved gases) in terms of variables, such as shear and stratification, that are easier to measure or explicitly include in regional numerical models. The observations presented here suggest division of the water column into three hydrodynamic regions of roughly equal depth: actively entraining surface and bottom boundary layers and a stratified midcolumn region between. For each region we have studied the dynamic causes and kinematic parameterizations of turbulence. Our main conclusions are as follows.

Turbulent entrainment at the base of a fluctuating wind-driven surface mixed layer was the largest source of vertical turbulent transport. The average diffusivity at the mixed layer base was $3 \times 10^{-4} \text{ m}^2 \text{ s}^{-1}$; the average buoyancy flux was $-4 \times 10^{-8} \text{ W kg}^{-1}$, comparable to the surface buoyancy input from solar heating (Figs. 1 and 6). Below the mixed layer entrainment zone, turbulence was an order of magnitude weaker except during periods of strong internal wave shear.

The relationship between midcolumn turbulence and internal wave shear can be divided into two dynamic regimes: one in which the energy-containing modes have subcritical Richardson numbers and produce strong turbulence and one in which the energy-containing modes are stable and lead to weaker turbulence through wave-wave interactions (section 4c). Below the surface mixed layer, the strongest turbulence occurred during the first week, in regions of subcritical Richardson numbers produced by shear from lowest-mode internal waves. For example, on yearday 118 mode-1 waves generated by a passing storm (MG05) led to an inverse Richardson number above 4 in most of the stratified water column and an associated average dissipation rate of $1.4 \times 10^{-7} \text{ W kg}^{-1}$ (Figs. 5 and 9). The associated average diffusivity, $1.8 \times 10^{-3} \text{ m}^2 \text{ s}^{-1}$, was strong enough to modify 10-m-tall scalar gradients over the course of a single day. The best predictor of the turbulent dissipation rate in this and similar cases was the dimensional scaling of KWB, which can be implemented in models and measurements that resolve vertical scales over which the Richardson number is unstable. Energetically, the rate of turbulence production was governed by external forcing mechanisms (wind stress or conversion of the barotropic tide) that generate internal waves.

As stratification grew, low-mode wave shear was no longer strong enough to produce subcritical Richardson numbers, and average turbulence dropped an order of magnitude (Fig. 9). Nevertheless, turbulence followed evolving patterns of low-mode shear and was concentrated in regions of high stratification (Fig. 2). Associated average diffusivities ranged from $5 \times 10^{-6} \text{ m}^2 \text{ s}^{-1}$ to $10^{\times 4} \text{ m}^2 \text{ s}^{-1}$. Statistical analysis shows dissipation to vary positively with both shear and stratification, in marked contrast to the predictions of the Gregg-Heney turbulence parameterization (Fig. 11). Instead, turbulence agreed well with the kinematic parameterization developed by MGa that adapts previous wave-wave interaction theories for the continental shelf environment.

A simple one-dimensional model of temperature evolution, driven by measured surface heat fluxes, observed mixed layer variability, and calculated turbulent diffusivities, accurately reproduces the transport of heat below the mixed layer during the first week (Fig. 12). In contrast, a similar model using a static mixed layer depth predicts unrealistically warm surface water above an overly sharp temperature gradient. In the second week, the one-dimensional model with a variable mixed layer still captures the essential temperature evolution, though strict comparison with data is hindered by advection of cool, fresh near-surface water.

The two dynamic turbulence regimes described here were present in both spring and summer observations. In particular, it is notable and surprising that a parameterization developed to relate turbulence to shear from an internal tide appears to work just as well relating turbulence to near-inertial internal waves. This robustness suggests that the results presented here and in MGa may be applicable in a wide range of shallow environments—wherever boundary layers are limited in extent and low frequency, low-vertical-mode internal waves proliferate.

Acknowledgments. We thank Jody Klymak, Earl Krause, Jack Miller, Gordon Welsh, and the entire crew of the R/V *Knorr* for help with data collection. Numerous other CMO investigators generously shared their thoughts and results with us. We particularly thank Tommy Dickey for sharing mooring data, as well as Wilf Gardner, Murray Levine, Tim Boyd, Jack Barth, Steve Anderson, Steve Lentz, and A1 Plueddemann. This work was supported by ONR Grant N00014-95-1-0406. Author J. MacKinnon received additional support from an NDSEG research fellowship; M. Gregg received additional support from the SECNAV/CNO Chair in Oceanography.

REFERENCES

- Aikman, F., III, 1984: Pycnocline development and its consequences in the Middle Atlantic Bight. *J. Geophys. Res.*, **89**, 685–694.
- Alford, M. H., and M. C. Gregg, 2001: Near-inertial mixing: Modulation of shear, strain and microstructure at low latitude. *J. Geophys. Res.*, **106** (C8), 16 947–16 968.
- Baumert, H., and H. Peters, 2000: Second-moment closures and length scales for weakly stratified turbulent shear flows. *J. Geophys. Res.*, **105** (C3), 6453–6468.
- Chang, G., and T. Dickey, 2001: Optical and physical variability on timescales from minutes to the seasonal cycle on the New England shelf: July 1996 to June 1997. *J. Geophys. Res.*, **106** (C5), 9435–9453.
- Chant, R. J., 2001: Evolution of near-inertial waves during an upwelling event on the New Jersey inner shelf. *J. Phys. Oceanogr.*, **31**, 746–764.
- Chapman, D. C., and R. C. Beardsley, 1989: On the origin of shelf water in the Middle Atlantic Bight. *J. Phys. Oceanogr.*, **19**, 384–391.
- , and G. Gawarkiewicz, 1993: On the establishment of the seasonal pycnocline in the Middle Atlantic Bight. *J. Phys. Oceanogr.*, **23**, 2487–2491.
- Chen, C., and L. Xie, 1997: A numerical study of wind-induced, near-inertial oscillations over the Texas-Louisiana shelf. *J. Geophys. Res.*, **102** (C7), 15 583–15 593.
- , R. O. Reid, and W. D. Nowlin Jr., 1996: Near-inertial oscillations of the Texas-Louisiana shelf. *J. Geophys. Res.*, **101** (C2), 3509–3524.
- Colosi, J., R. C. Beardsley, J. Lynch, G. Gawarkiewicz, C.-S. Chiu, and A. Scotti, 2001: Observations of nonlinear internal waves on the outer New England continental shelf during summer shelfbreak primer. *J. Geophys. Res.*, **106** (C5), 9587–9602.
- D'Asaro, E. A., and R.-C. Lien, 2000: The wave–turbulence transition for stratified flows. *J. Phys. Oceanogr.*, **30**, 1669–1678.
- Dewey, R. K., and W. R. Crawford, 1988: Bottom stress estimates from vertical dissipation rate profiles on the continental shelf. *J. Phys. Oceanogr.*, **18**, 1167–1177.
- Dickey, T. D., and A. J. Williams III, 2001: Interdisciplinary ocean process studies on the New England shelf. *J. Geophys. Res.*, **106**, 9427–9434.
- Dillon, T. M., 1982: Vertical overturns: A comparison of Thorpe and Ozmidov length scales. *J. Geophys. Res.*, **87**, 9601–9613.
- Gardner, W., and Coauthors, 2001: Optics, particles, stratification, and storms on the New England continental shelf. *J. Geophys. Res.*, **106**, 9473–9497.
- Gregg, M. C., 1989: Scaling turbulent dissipation in the thermocline. *J. Geophys. Res.*, **94** (C7), 9686–9698.
- Hebert, D., and J. Moum, 1994: Decay of a near-inertial wave. *J. Phys. Oceanogr.*, **24**, 2334–2351.
- Heney, F. S., J. Wright, and S. M. Flatté, 1986: Energy and action flow through the internal wave field. *J. Geophys. Res.*, **91**, 8487–8495.
- Holloway, P. E., P. G. Chatwin, and P. Craig, 2001: Internal tide observations from the Australian North West Shelf in summer 1995. *J. Phys. Oceanogr.*, **31**, 1182–1199.
- Inall, M. E., T. P. Rippeth, and T. J. Sherwin, 2000: The impact of non-linear waves on the dissipation of internal tidal energy at a shelf break. *J. Geophys. Res.*, **105** (C4), 8687–8705.
- Ivey, C., and J. Imberger, 1991: On the nature of turbulence in a stratified fluid. Part I: The energetics of mixing. *J. Phys. Oceanogr.*, **21**, 650–658.
- Kunze, E., A. J. Williams III, and M. G. Briscoe, 1990: Observations of shear and vertical stability from a neutrally buoyant float. *J. Geophys. Res.*, **95** (C10), 18 127–18 142.
- Ledwell, J., T. Duda, M. Sundermeyer, and H. Seim, 2004: Mixing in a coastal environment part I: A view from dye dispersion. *J. Geophys. Res.*, **109**, C10013, doi:10.1029/2003JC002194.
- Lentz, S., K. Shearman, S. Anderson, A. Plueddemann, and J. Edson, 2003: Evolution of stratification over the New England shelf during the Coastal Mixing and Optics study, August 1996–June 1997. *J. Geophys. Res.*, **108**, 3008, doi:10.1029/2001JC001121.
- Linder, C. A., and G. Gawarkiewicz, 1998: A climatology of the shelfbreak front in the Middle Atlantic Bight. *J. Geophys. Res.*, **103** (C9), 18 405–18 423.
- Loder, J. W., B. Petrie, and G. Gawarkiewicz, 1998: The coastal ocean off northeastern North America: A large-scale view. *The Sea*, A. R. Robinson and K. H. Brink, Eds., Vol. 11, The Global Coastal Ocean: Regional Studies and Syntheses, John Wiley and Sons, 105–133.
- Lombardo, C., and M. Gregg, 1989: Similarity scaling of viscous a thermal dissipation in a convecting surface boundary layer. *J. Geophys. Res.*, **94** (C5), 6273–6284.
- MacKinnon, J., and M. Gregg, 2003a: Mixing on the late-summer New England shelf—Solibores, shear, and stratification. *J. Phys. Oceanogr.*, **33**, 1476–1492.
- , and —, 2003b: Shear and baroclinic energy flux on the summer New England shelf. *J. Phys. Oceanogr.*, **33**, 1462–1475.
- , and —, 2005: Near-inertial waves on the New England shelf: The role of evolving stratification, turbulent dissipation, and bottom drag. *J. Phys. Oceanogr.*, **35**, 2408–2424.
- Moum, J. N., 1996: Energy-containing scales of turbulence in the ocean thermocline. *J. Geophys. Res.*, **101** (C6), 14 095–14 109.
- , D. Farmer, W. Smyth, L. Armi, and S. Vagle, 2003: Structure and generation of turbulence at interfaces strained by internal solitary waves propagating shoreward over the continental shelf. *J. Phys. Oceanogr.*, **33**, 2093–2112.
- Nash, J. D., and J. N. Moum, 2001: Internal hydraulic flows on the continental shelf: High drag states over a small bank. *J. Geophys. Res.*, **106** (C3), 4593–4612.
- Oakey, N. S., 1982: Determination of the rate of dissipation of turbulent energy from simultaneous temperature and velocity shear microstructure measurements. *J. Phys. Oceanogr.*, **12**, 256–271.
- , and B. J. W. Greenan, 2004: Mixing in a coastal environment: 2. A view from microstructure measurements. *J. Geophys. Res.*, **109**, C10014, doi:10.1029/2003JC002193.
- Osborn, T. R., 1980: Estimates of the local rate of vertical diffusion from dissipation measurements. *J. Phys. Oceanogr.*, **10**, 83–89.
- Ou, H., and R. Houghton, 1982: A model of the summer progression of the cold-pool temperature in the Middle Atlantic Bight. *J. Phys. Oceanogr.*, **12**, 1030–1036.
- Polzin, K., 1996: Statistics of the Richardson number: Mixing models and finestructure. *J. Phys. Oceanogr.*, **26**, 1409–1425.
- , J. M. Toole, and R. W. Schmitt, 1995: Finescale parameterizations of turbulent dissipation. *J. Phys. Oceanogr.*, **25**, 306–328.
- Rehmann, C. R., and T. F. Duda, 2000: Diapycnal diffusivity inferred from scalar microstructure measurements near the New England shelf/slope front. *J. Phys. Oceanogr.*, **30**, 1354–1371.
- Rippeth, T. P., and M. E. Inall, 2002: Observations of the internal

- tide and associated mixing across the Malin shelf. *J. Geophys. Res.*, **107**, 3028, doi:10.1029/2000JC000761.
- Sandstrom, H., and J. Elliot, 1984: Internal tide and solitons on the Scotian shelf: A nutrient pump at work. *J. Geophys. Res.*, **89**, 6415–6426.
- , and N. Oakey, 1995: Dissipation in internal tides and solitary waves. *J. Phys. Oceanogr.*, **25**, 604–614.
- Sharples, J., C. M. Moore, and E. R. Abraham, 2001: Internal tide dissipation, mixing, and vertical nitrate flux at the shelf edge of NE New Zealand. *J. Geophys. Res.*, **106** (C7), 14 069–14 081.
- Shaw, W. J., J. H. Trowbridge, and A. J. Williams III, 2001: Budgets of turbulent kinetic energy and scalar variance in the continental shelf bottom boundary layer. *J. Geophys. Res.*, **106** (C5), 9551–9564.
- Shearman, R. K., 2005: Observations of near-inertial current variability on the New England shelf. *J. Geophys. Res.*, **110**, C02012, doi:10.1029/2004JC002341.
- Simpson, J. H., W. R. Crawford, T. P. Rippeth, A. R. Campbell, and J. V. S. Cheok, 1996: The vertical structure of turbulent dissipation in shelf seas. *J. Phys. Oceanogr.*, **26**, 1579–1590.
- Sosik, H., R. Green, W. Pegau, and C. Roesler, 2001: Temporal and vertical variability in optical properties of New England shelf waters during late summer and spring. *J. Geophys. Res.*, **106** (C5), 9455–9472.
- Sun, H., and E. Kunze, 1999: Internal wave–wave interactions. Part II: Spectral energy transfer and turbulence production rates. *J. Phys. Oceanogr.*, **29**, 2905–2919.
- van Haren, H., L. Mass, J. Zimmerman, H. Ridderinkhof, and H. Malschaert, 1999: Strong inertial currents and marginal internal wave stability in the central North Sea. *Geophys. Res. Lett.*, **26**, 2993–2996.
- Veronis, G., 1972: On properties of seawater defined by temperature, salinity and pressure. *J. Mar. Res.*, **90**, 227–255.
- Wesson, J. C., and M. C. Gregg, 1994: Mixing at Camarinal sill in the Strait of Gibraltar. *J. Geophys. Res.*, **99** (C5), 9847–9878.